

Interpretation of a multicomponent walkaway vertical seismic profile data

Bona Wu, Don C. Lawton, and Kevin W. Hall

ABSTRACT

A multicomponent walkaway VSP data was processed to study the AVO response. Inversion and AVO modeling were conducted on PP wave data. The data show a Class I AVO response at the top of reservoir and a Class IV water-sand AVO response at the bottom of the study reservoir. There were no obvious gas effects in the study interval. The observations were validated by production data. Post stack PP-PS joint inversion was completed and compared to only P-wave inversion. Overall, they showed good consistency and the joint inversion added value to lithology prediction and fluid identification. This case study demonstrated that the multicomponent VSP is an effective tool to predict rock properties, characterize the reservoir and monitor production.

INTRODUCTION

This study is a continued work of a multicomponent walkaway VSP data analysis. For the details of acquisition and processing, please refer to Wu et al. (2014). Due to its geometry, a VSP survey usually yields higher resolution and signal-to-noise ratio than surface seismic data. In addition, the walkaway VSP geometry is suitable for AVO analysis. In this work, different types of rock properties were inverted from the VSP PP and PS image and prestack gathers. Interpretation of inversion and AVO modeling results helped us to better characterize the target reservoir and gave promise about how to integrate multicomponent VSP data into reservoir predicting and production monitoring.

The reservoir studied is relatively shallow (about 500m) and is made up of relatively unconsolidated shale-sand sequences, where fluid compressibility can have significant effect on the whole rock compressibility, which is then reflected on seismic data. The thickness of target reservoir is 50-75m which is suitable for studying the AVO responses. Since the well logs used in this study offset 200m from VSP borehole, detailed interpretations may be less reliable. However, the AVO analysis still might be used as a scanning procedure to highlight possible anomalies and indicate potential hydrocarbon.

AVO ANALYSIS

Principles of AVO analysis

AVO is an adaptive technique. The most common method of using AVO for interpretation of fluid and rock properties from seismic is the use of two-term approximations. The linear combination of intercept and gradient is the basis of fluid and rock discrimination from seismic.

In this work, the popular attributes applied in industry were applied in the target reservoir analysis and were listed in Table 1. The principles of each attribute were briefly introduced as follows.

Table 1. AVO attributes studied in this work

	Two-term Aki-Richard	Two-term Fatti method
Attributes	Intercept A	Rp0
	Gradient B	Rs0
Derived attributes	AVO product: A*B	Fluid Factor
	Poisson's Ratio: A+B	Lambda-Mu-Rho
	Shear wave reflectivity A-B	

*Intercept A, Gradient B, and AVO product A*B:*

Wiggins' form (1986) of Aki-Richard equation is:

$$R_{\theta} = A + B \sin^2 \theta \quad (1)$$

where:

$$A = \left[\frac{\Delta V_p}{2V_p} + \frac{\Delta \rho}{2\rho} \right] \text{ and } B = \frac{\Delta V_p}{2V_p} - 4 \left[\frac{V_s}{V_p} \right]^2 \frac{\Delta V_s}{V_s} - 2 \left[\frac{V_s}{V_p} \right]^2 \frac{\Delta \rho}{\rho}$$

A is called the intercept, B the gradient, and the A*B called AVO product.

Poisson's Ratio: A+B

Shuey's equation (1985) is:

$$B = A \left[D - 2(1+D) \frac{1-2\sigma}{1-\sigma} \right] + \frac{\Delta \sigma}{(1-\sigma)^2},$$

$$\text{where: } D = \frac{\Delta V_p / V_p}{\Delta V_p / V_p + \Delta \rho / \rho}, \sigma = \frac{\sigma_2 + \sigma_1}{2}, \text{ and } \Delta \sigma = \sigma_2 - \sigma_1 \quad (2)$$

The equation can be simplified by assuming $\sigma = 1/3$:

$$B = 2.25\Delta\sigma - A \quad (3)$$

or

$$A + B = 2.25\Delta\sigma \quad (4)$$

Therefore, the sum A+B proportional to the change in Poisson's Ratio.

Shear reflectivity A-B:

From question (1), if we assume $\frac{V_s}{V_p} = 1/2$, then:

$$B = \frac{\Delta V_p}{2V_p} - \frac{\Delta V_s}{V_s} - \frac{\Delta \rho}{2\rho} = R_{p0} - 2R_{s0} \quad (5)$$

where :

$$R_{p0} = A = \left[\frac{\Delta V_p}{2V_p} + \frac{\Delta \rho}{2\rho} \right] \text{ and } R_{s0} = \left[\frac{\Delta V_s}{V_s} + \frac{\Delta \rho}{\rho} \right]$$

$$\text{or: } R_s = 0.5(A - B) \quad (6)$$

Therefore, the difference A-B is proportional to the shear reflectivity.

$R_p(0^\circ)$ and $R_s(0^\circ)$:

The Fatti et al.(1994) approach rewritten the two term Aki-Richards equation as:

$$R_p(\theta) = c_1 R_p(0^\circ) + c_2 R_s(0^\circ) \quad (7)$$

$$\text{Where } R_p(0^\circ) = \frac{1}{2} \left[\frac{\Delta V_p}{V_p} + \frac{\Delta \rho}{\rho} \right] \text{ and } R_s(0^\circ) = \frac{1}{2} \left[\frac{\Delta V_s}{V_s} + \frac{\Delta \rho}{\rho} \right]$$

Which gives us a way to calculate $R_p(0^\circ)$ and $R_s(0^\circ)$ from seismic data.

Fluid factor:

Castagna's mudrock equation (1985) was assumed to be true for non-hydrocarbon filled layers, which is: $V_p = 1.16V_s + 1360m/s$

Smith and Gidlow (1987) and Fatti et al. (1994) derived the fluid factor attribute is based on above equation which is:

$$\Delta F = \frac{\Delta V_p}{V_p} - 1.16 \left(\frac{V_s}{V_p} \right) \frac{\Delta V_s}{V_s}, \text{ or } \Delta F = R_p - 1.16 \left(\frac{V_s}{V_p} \right) R_s \quad (8)$$

The fluid factor highlights layers where Castagna's equation doesn't fit, such as potential hydrocarbon zones.

Lambda-Mu-Rho (LMR):

Goodway et al. (1997) proposed a new approach to AVO inversion based on the Lamé parameters λ and μ , and density ρ , or Lambda-Mu-Rho (LMR).

$$\text{From } V_s = \sqrt{\frac{\mu}{\rho}} \quad (9)$$

$$\text{and } V_p = \sqrt{\frac{\lambda + 2\mu}{\rho}} \quad (10)$$

we can derive:

$$\begin{aligned}\mu\rho &= Z_s^2 \\ \lambda\rho &= Z_p^2 - 2Z_s^2\end{aligned}\tag{11}$$

Where: Z_p is P wave impedance and Z_s is Shear wave impedance.

Therefore, crossplot $\lambda\rho$ vs $\mu\rho$ can minimize the effects of density and help to interpret the λ and μ attributes: the λ term (incompressibility) is sensitive to the pore fluid, whereas the μ term (rigidity) is sensitive to rock matrix.

AVO classification:

AVO classes as published describe AVO responses only for single interface (e.g. Simm and Bacon, 2014). The classification works well for thick-bedded sand settings and becomes less useful in reservoir sections with multiple thin beds. In this work, the reservoir is a sand/shale system with average thickness of 50-75m, which is adequate for AVO analysis. Both the top and bottom interfaces were studied.

Rutherford and Williams (1989) derived the following classification scheme for AVO anomalies, with further modifications by Ross and Kinman (1995) and Castagna (1997): Class 1: High impedance sand with decreasing AVO; Class 2: Near-zero impedance contrast; Class 2p: Same as 2, with polarity change; Class 3: Low impedance sand with increasing AVO; Class 4: Low impedance sand with decreasing AVO. The classification is listed in Table 2 and the distribution of AVO anomalies on Gradient-Intercept crossplot system is shown in Figure 1.

Table 2. AVO classification

	Impedance compare to encasing shale	Amplitude vs offset
CLASS I	Higher impedance	Reduce
CLASS II	Similar but lower	Increase
CLASS IIp	Similar but higher	Increase
CLASS III	Lower	Increase
CLASS IV	Lower	Decrease

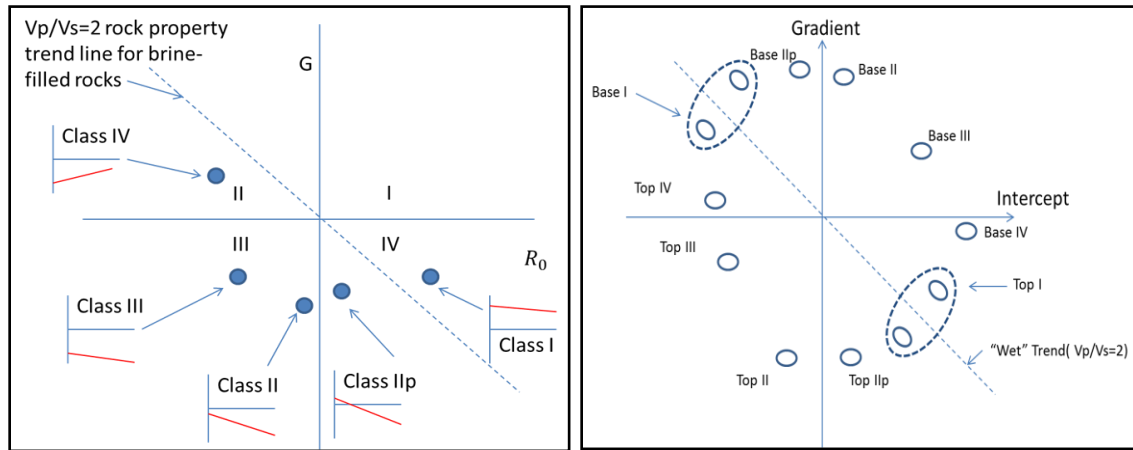


FIG. 1. Top sand AVO responses on the crossplot (modified after Castagna et al. quadrant numbering system, 1998).

Theory of AVO modeling

AVO modeling was applied to identify the scenarios which caused AVO responses including the seismic velocities, density of the reservoir and pore fluids. The principle of AVO modeling is Gassmann's equations (Gassmann, 1951) which relate the bulk modulus of a rock to its pore, frame, and fluid properties. The equation is given as:

$$K_{sat} = K_{frame} + \frac{\left(1 - \frac{K_{frame}}{K_{matrix}}\right)^2}{\frac{\phi}{K_{fluid}} + \frac{(1-\phi)}{K_{matrix}} \frac{K_{frame}}{K_{matrix}^2}} \quad (12)$$

Where, K_{sat} , K_{frame} , K_{matrix} , and K_{fluid} are the bulk moduli of the saturated rock, porous rock frame, mineral matrix, and pore fluid, respectively and ϕ is porosity. In this equation, the shear modulus is independent of pore fluid and held constant during the fluid substitutions.

The bulk modulus (K_{sat}) and shear modulus (μ) at in-situ condition can be estimated from log following formula:

$$K_{sat} = \rho \left(V_p^2 - \frac{4}{3} V_s^2 \right) \quad (13)$$

and

$$\mu = \rho V_s^2 \quad (14)$$

If there isn't V_s log, it can be estimated from Castagna assumption.

By giving mineral composition of rock, we can calculate the modulus of mineral matrix and density. Similarly, we can obtain bulk modulus and density of pore fluid. Then, K_{frame} can be estimated from equation (12). Therefore, if we change the fluid content of reservoir and estimate the bulk modulus and density of desired fluid, then we can substitute those values to equation (12) to calculate the new bulk modulus and velocities of the saturated rock after fluid substitution.

FIELD DATA INTERPRETATION

Geology background in the study area

The study formation is a heavy oil reservoir in Canada. It was deposited as prograding tide-dominated deltas and composed of three stacked incised valleys. These incised valleys lie encased within more regional deltaic, shoreface sands and marine muds. Total thickness of the study formation is approximately 50-75 meters (Hein et al., 2007) and it is an important resource of 9-10⁰ API bitumen. The field is actively produced by steam assistant gravity drainage (SAGD).

The typical well log in this area is shown in Figure 2. In the reservoir zone, the Gamma Ray values are low which indicates clean sand deposits. High resistivity and porosity in these zones also indicate a good hydrocarbon reservoir. At the bottom of sand filled valley, the resistivity becomes lower, which indicates bottom water. Above the bottom water zone is the transition zone.

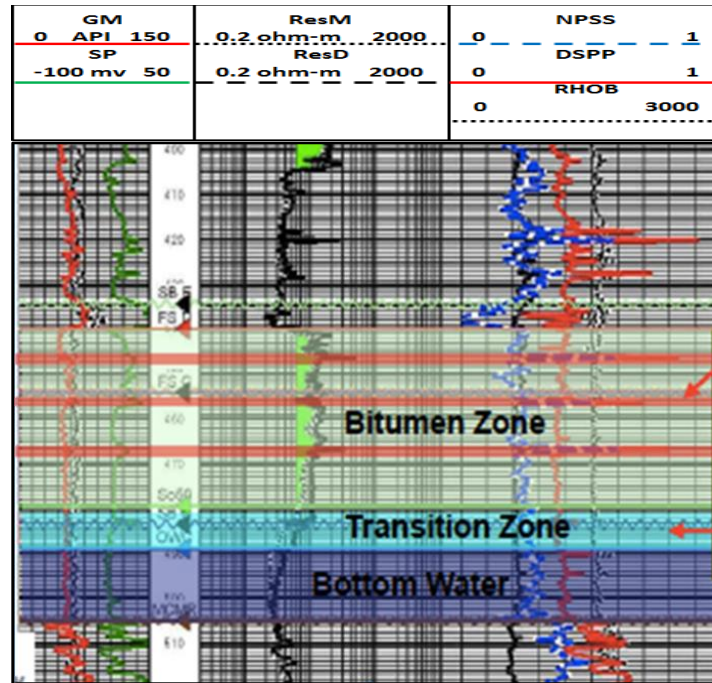


FIG. 2. Typical log of study reservoir (picture from AER report).

Inversion and AVO attributes analysis

Figure 3 shows statistical wavelet and correlation of VSP trace with synthetic seismogram. The wavelet was extracted from VSP-CDP mapping image (Figure 3a) and correlation analysis window is in the reservoir zone (430-510ms, marked in Figure 3b). In Figure 3b, the red cloumm are the VSP traces close to well location and blue column are synthetic traces. The VSP and synthetic seismograms show excellent alignment. Figure 4a shows poststack inversion analysis. From left to right, the columns are impedance log, statistical wavelet, synthetic and seismic traces, followed by the error between systhetic and seismic. Small errors indicate reliable inversion result. Figure 4b shows inverted P-impedance. The shale/sand contact of reservoir top (around 440ms)

changes at the top of the reservoir due to small changes of density and shear wave velocity, but it shows increasing S-impedance at the bottom of the study interval.

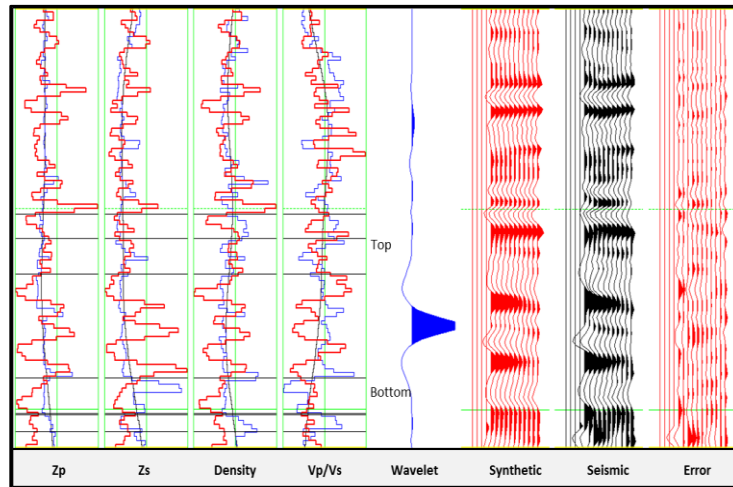


FIG. 5. Prestack inversion analysis. From left to right, are the inversion results (in red) Z_p , Z_s , Density, V_p/V_s respectively overlaying the original logs from the well (blue), black curves are original model; next are synthetic traces (in red) followed by the VSP angle gather (in black), and errors between inverted synthetic and seismic.

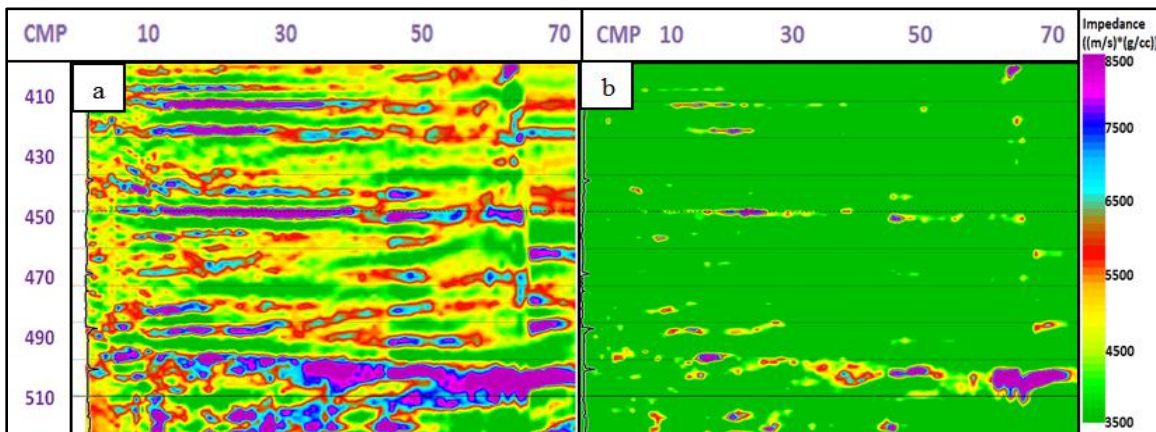


FIG. 6. (a) Inverted P-wave impedance and (b) S-wave impedance.

Figure 7 is S-impedance vs P-impedance crossplot. The samples from the reservoir top are highlighted by a red ellipse while the samples from the base of the reservoir are highlighted by a yellow ellipse. Apparently, the reservoir bottom has a higher Z_s/Z_p . The crossplot canceled out the effect of density (assume density has negligible changes). Therefore, it is reciprocal of V_p/V_s ratio which is higher at top of reservoir and lower at bottom of reservoir and they both follow an approximately linear trend. The decreased V_p/V_s ratio indicates saturation of hydrocarbon. Figure 8 shows the inverted density and V_p/V_s . Density doesn't show big differences inside the reservoir while V_p/V_s ratio does. Above and at the top of the reservoir (450ms), the V_p/V_s values are relatively high while at the base of the reservoir, the V_p/V_s ratios are low (green). The results are consistent with observations of Z_s vs Z_p crossplot shown in Figure 7.

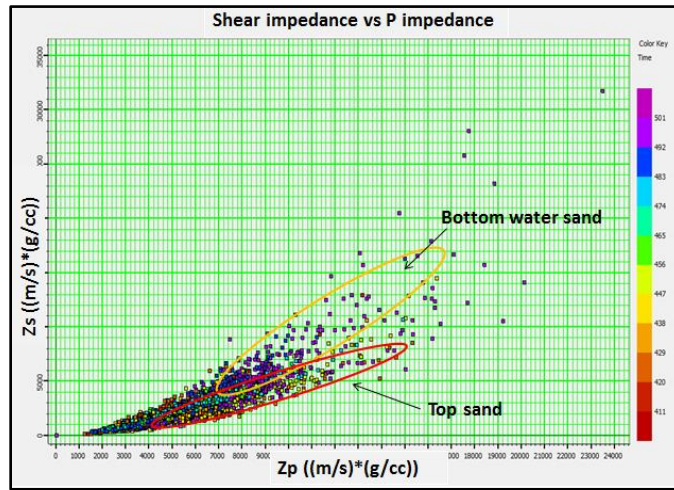


FIG. 7. S-wave impedance vs P-wave impedance crossplot.

V_p/V_s is also a good indicator of the sand and shale distribution. Based on Greenberg and Castagna’s (1992) definition of different for commonly occurring lithologies, sand has slightly higher V_p/V_s than shale. However, the entire reservoir zone (sand, 450ms - 500ms) shows lower values of V_p/V_s which indicates saturation of hydrocarbon or water. With present of water or oil, V_p/V_s is decreasing. Bottom of reservoir shows lowest V_p/V_s ratio. If gas is present, the V_p/V_s is even lower than for wet sands. We need to combine other information to eliminate the ambiguous and obtain a valid prediction. Be note, the density section doesn’t show obvious lateral variations but V_p/V_s does, which indicates lateral change of reservoir lithology or fluid.

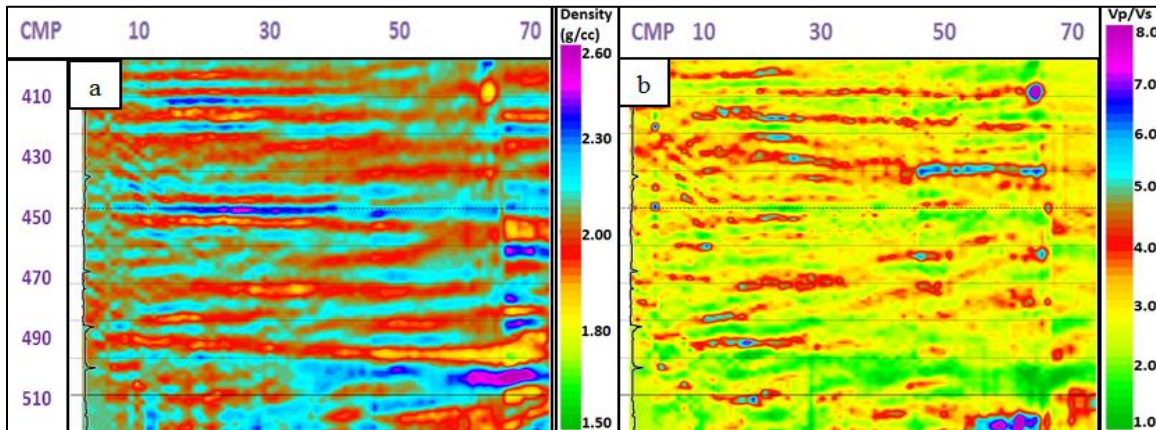


FIG. 8. (a) Inverted density and (b) V_p/V_s ratio.

V_p/V_s vs P-wave impedance crossplot (Figure 9) shows the top and bottom trend of the study reservoir. Most of samples from the reservoir top (shale-sand contact, yellow and orange dots) are located in low impedance but high V_p/V_s zone while samples from the bottom of the reservoir (sand-shale contact, purple dots) are located in high P-impedance but low V_p/V_s zone. The analysis is consistent with observations discussed above (Figure 6 to Figure 8). The crossplot also makes easier for us to identify the gas effects. If there is gas effect, it should locate at low P-wave impedance and low V_p/V_s

zone (left bottom corner, marked by blue circle). Apparently, in our study reservoir, there are no gas effects.

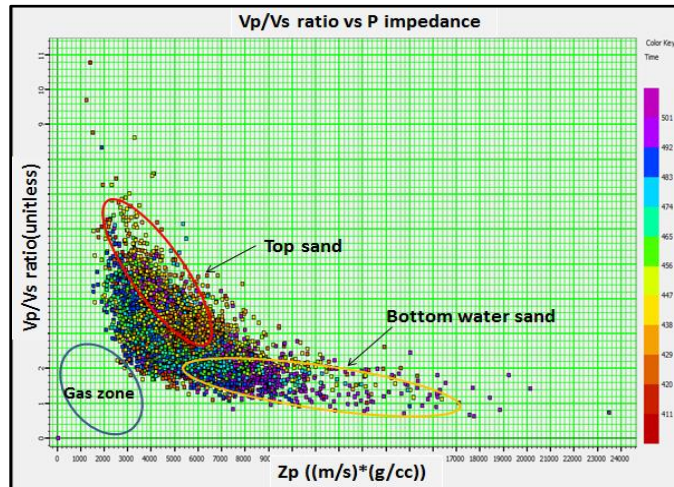


FIG. 9. Vp/Vs ratio vs P-wave impedance crossplot.

P-wave AVO attributes analysis

The processed far offset shots were used to create a reflectivity gather for AVO analysis. The workflow and parameters are discussed by Wu et al., 2014. Figure 10a shows the correlation between the reflectivity gather and the synthetic seismogram around the reservoir zone. The seismogram was created by the CREWES tool Syngram. The top and bottom of the target reservoir show good correlation while inside the reservoir, the amplitude and phases of the VSP data show some differences from the synthetic seismogram. The distance between logged well and VSP borehole is one possible reason of this mis-tie. In addition to that, the well was logged in 1980's before steam injection, therefore, we expect to see reservoir changes after steaming and production. The AVO responses of the target reservoir are shown in Figure 10b. Overall, the amplitudes picked from VSP and synthetic seismogram at the top and bottom of the reservoir display a similar trend within an offset range of 0 to 600 m. At the top, the amplitudes are positive and decrease with offset, whereas at the bottom, the amplitudes are negative but also decrease with offset.

The AVO gather was then transformed to angle gathers to undertake AVO attributes analysis in Hampson-Russell software (Figure 11). Red squares are amplitudes extracted from VSP angle gathers and solid lines are plots of Aki-Richard two-term equation. The fit of the AVO curves is extremely good. At the top and bottom of the reservoir, both amplitudes of VSP data show decreasing along the incident angle which is similar trend as seen in synthetic seismic data. The top interface falls into Class I AVO response while the base falls into Class IV AVO responses.

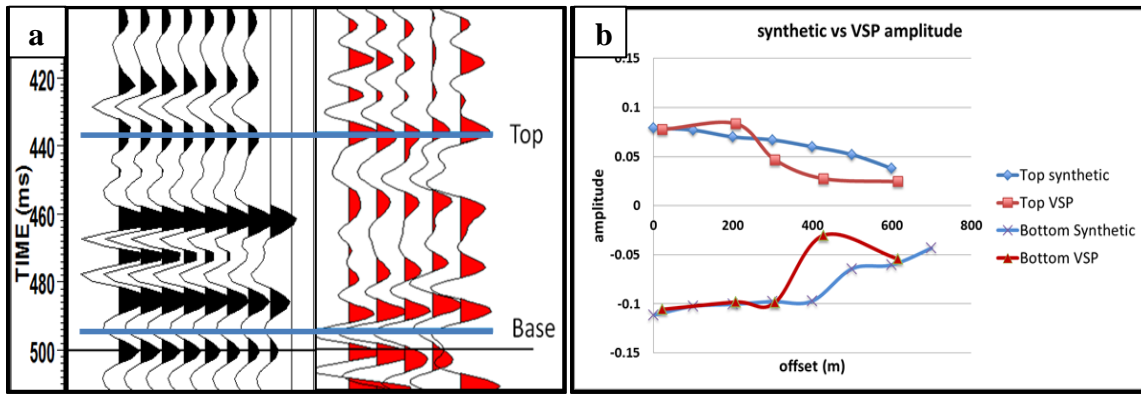


FIG. 10. (a) Tie of synthetic offset gather (shown in black) and reflectivity gather (shown in red). Top and bottom of the target reservoir are picked and highlighted by blue lines. (b) AVO responses at top and base of study reservoir. Red lines are amplitudes from VSP and blue lines are amplitudes from synthetic seismogram.

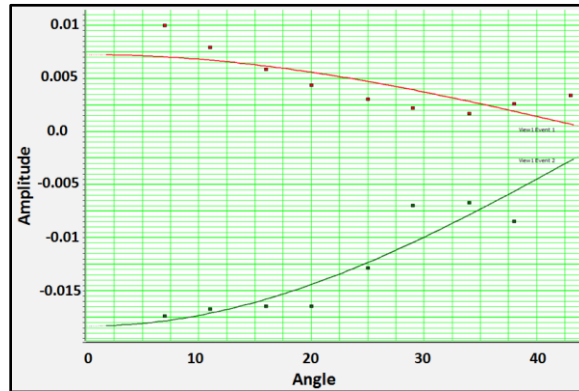


FIG. 11. Gradient curve. Dots curves are amplitudes measured from the VSP gather and solid lines are amplitudes measured from the synthetic seismogram. Red curve and dots are from the top of the reservoir and green curves and dots are from the bottom of the reservoir.

Figure 12 shows AVO attributes derived from the CMP gathers from the VSP data, based on two-term Aki-Richards equation. From left to right, are intercept A, gradient B, AVO product $A*B$, scaled Poisson's ratio $(aA+bB)$, and scaled shear reflectivity $(aA-Bb)$ separately. At the top of the reservoir (440ms, sand), the intercept is positive while at the base of the reservoir (495ms), the intercept is negative. The gradient value is small in the entire study zone. AVO product at the top (440ms) and the base of the reservoir (495ms) are “dim” or “negative” responses. Scaled Poisson's ratio is negative (light green) at top which indicating a drop in Poisson's ratio and positive (yellow) at the base of the reservoir, indicating an increase in Poisson's ratio. Scaled shear wave reflectivity is positive at top but negative at bottom.

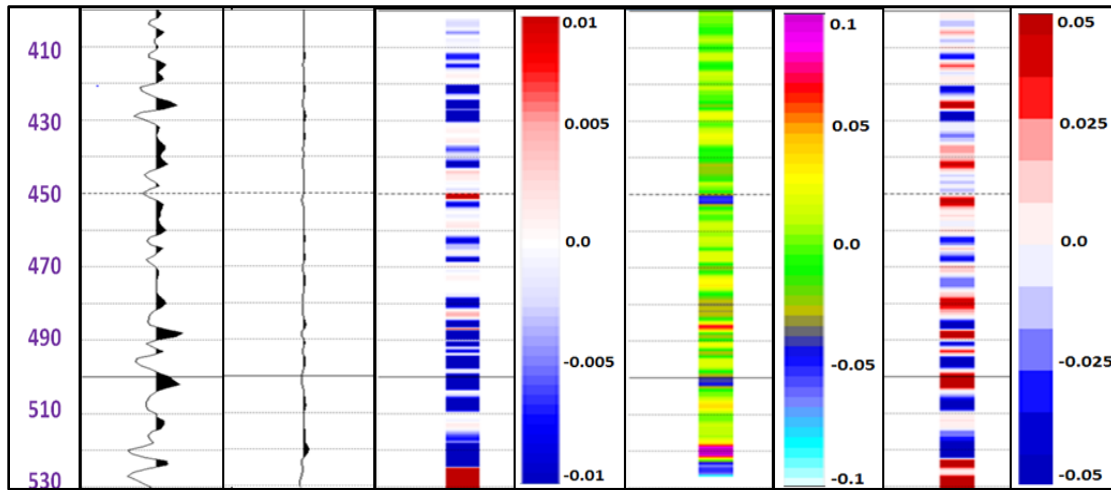


FIG. 12. From left to right, are intercept A, gradient B, AVO product $A*B$, scaled Poisson's ratio ($aA+bB$), and scaled shear reflectivity ($aA-Bb$) from two-term Aki-Richards method (angle gather is up to 42 degree).

Two-term Fatti equation gives us other attributes and a more accurate estimate of S-wave reflectivity, shown in Figure 13. Both R_{p0} and R_{s0} are positive at the top of the reservoir and negative at the base of the reservoir. Inside the reservoir, we see a large decrease of P-wave reflectivity while less of a change in S-wave reflectivity. Low values (anomalies) of fluid factor show small deviation from the mudrock trend at the top and bottom of the reservoir (close to zero).

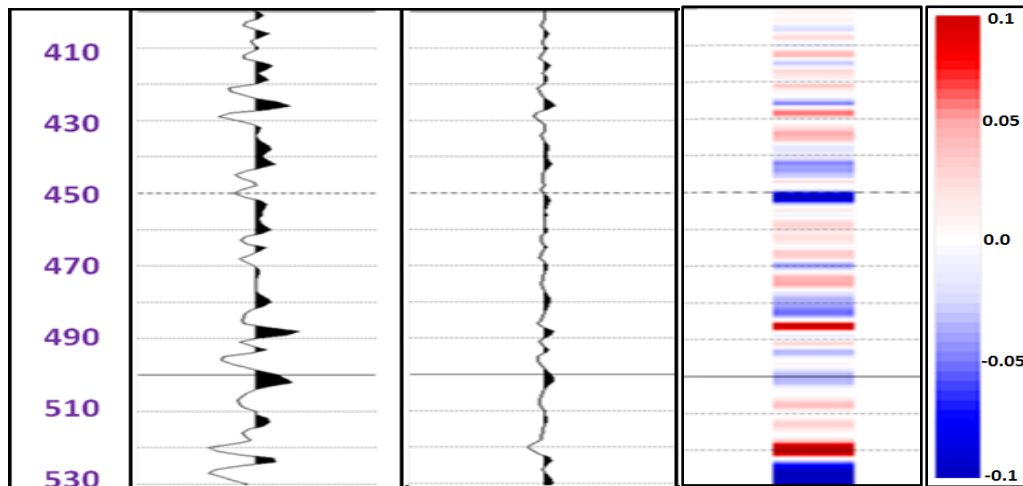


FIG. 13. From left to right, are P-wave reflectivity R_{p0} and S-wave reflectivity R_{s0} from two-term Fatti's method, and derived fluid factor at $Vp/Vs=2.0$.

From the above analysis, at the top of the reservoir, the shale-sand interface has a positive impedance change and a negative Poisson's ratio change, which gives a negative AVO gradient (class I response). At the base of the reservoir, the impedance decreases but Poisson's ratio increases due to existence of water in the pore space (Carcione and Cavallini, 2002), which is a Class IV AVO response. All the parameters are summarized and listed in Table 3.

Table 3. Properties of study reservoir

Reservoir	Top	Base
Interface	shale-sand	sand-shale
Impedance change	+ve	-ve
Amplitude	+ve	-ve
Amplitude change	Decreases with offset	Decreases with offset
Poisson's ratio	Decrease	Increase
AVO classification	I	IV
Wet sand, no gas response		

Similarly, we derived AVO attributes from the CMP gathers of the entire survey and they are shown in Figure 14 to Figure 20. All the attributes show similar signatures at the well location as the attributes from single CMP discussed above but also display lateral variations along the survey.

In the study reservoir, at the top, the intercept A represents zero-offset reflection coefficient shown in Figure 14a. It is positive (red) at top and negative at bottom (blue). While gradient B (Figure 14b) is negative (blue) at top but positive (red) bottom. The gradient vs intercept crossplot (Figure 15) shows all the samples inside the reservoir distribute along the linear wet trend ($V_p/V_s=2.0$) which indicates no gas anomaly.

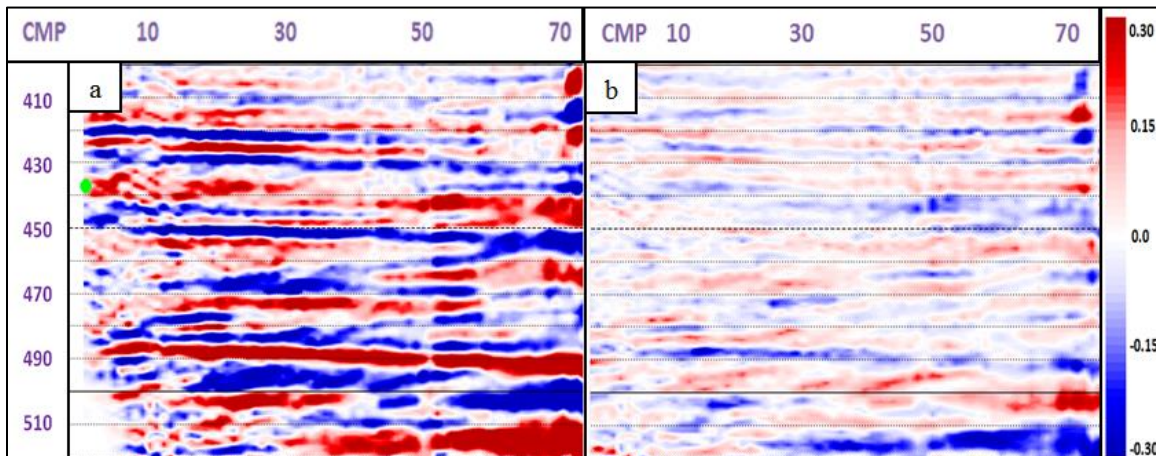


FIG. 14. (a) Intercept A and (b) gradient B from Aki- Richard equation.

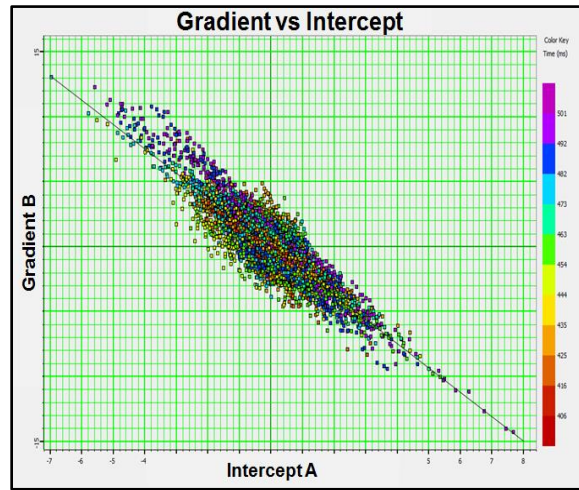


FIG. 15. Gradient (B) vs Intercept (A) crossplot.

Figure 16a is AVO product $A*B$. Negative AVO production values indicate decreasing amplitude with offset which is class I or Class IV AVO response. Around CMP 30, at 455ms, the weak red colour (highlighted by red circle) indicates potential thin Class II or Class III AVO effects which both show increasing amplitude with offset. The positive AVO product can be a soft marker of hydrocarbon. Figure 16b shows decreasing Poisson's ratio (blue to green/orange, highlighted by red rectangle) at the top of the reservoir while increasing in Poisson's ratio at the bottom of the reservoir (green/orange to blue/yellow, highlighted by blue rectangle).

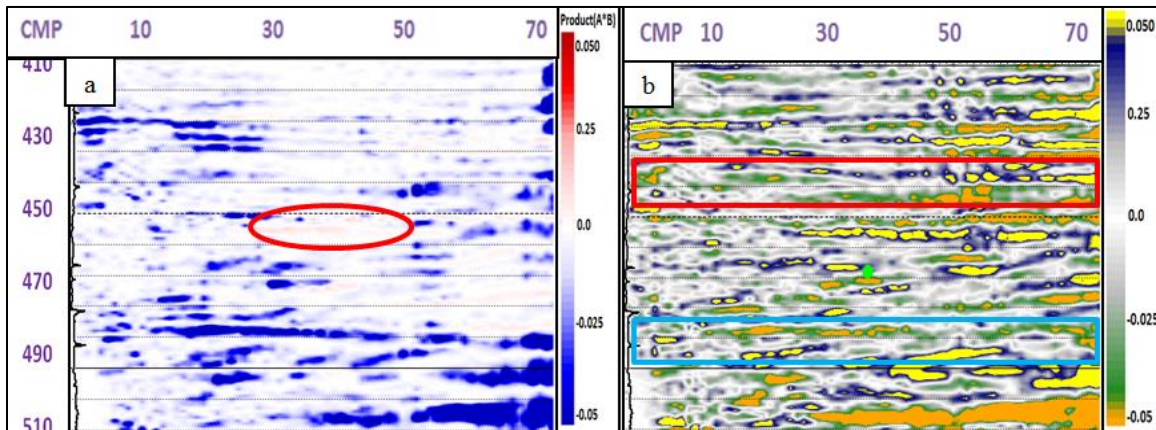


FIG. 16. AVO product $A*B$ and scaled Poisson's ratio.

Figure 17 shows R_s and R_p crossplot which are derived from Fatti equation. We can see two trends with small difference in slope which are highlighted by red and yellow dotted lines. Samples along red line are mostly from the top of the reservoir and samples along yellow line are mostly from the base of the reservoir. The different slopes indicate the reservoir top has a lower R_p/R_s than the base.

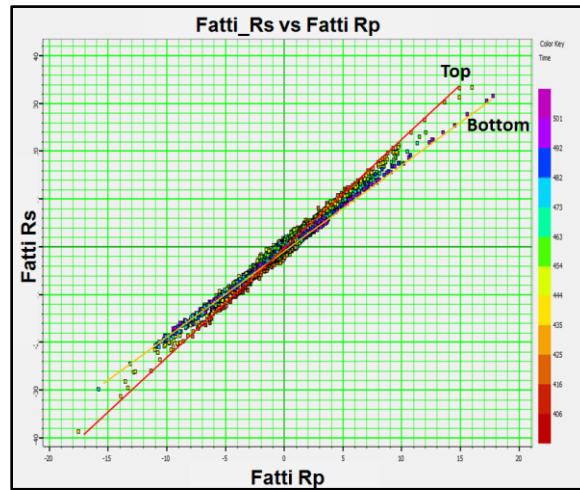


FIG. 17. Rs vs Rp cross plot.

As inputs to poststack inversion, we can derive Z_p and Z_s from R_p and R_s which are shown in Figure 18. The inverted P impedance shows similar signature as post-stack and pre-stack inversion results (Figure 4b and Figure 6a). Figure 18 shows at the top of the reservoir, there is not a big difference above and below the shale-sand interface. But at the bottom of the reservoir, the sand-shale contact shows an obvious increase of S-impedance. Figure 19 is Z_s vs Z_p crossplot. The crossplot shows that the top sand has higher Z_p/Z_s ratio and the bottom water sand has lower Z_p/Z_s ratio. Inside the reservoir, sand samples show both low Z_p and Z_s .

Figure 20 shows angle gathers and inverted fluid factor. Fluid factor shows increasing deviation with increasing distance from the VSP borehole. This may indicate potential hydrocarbons in far offset locations.

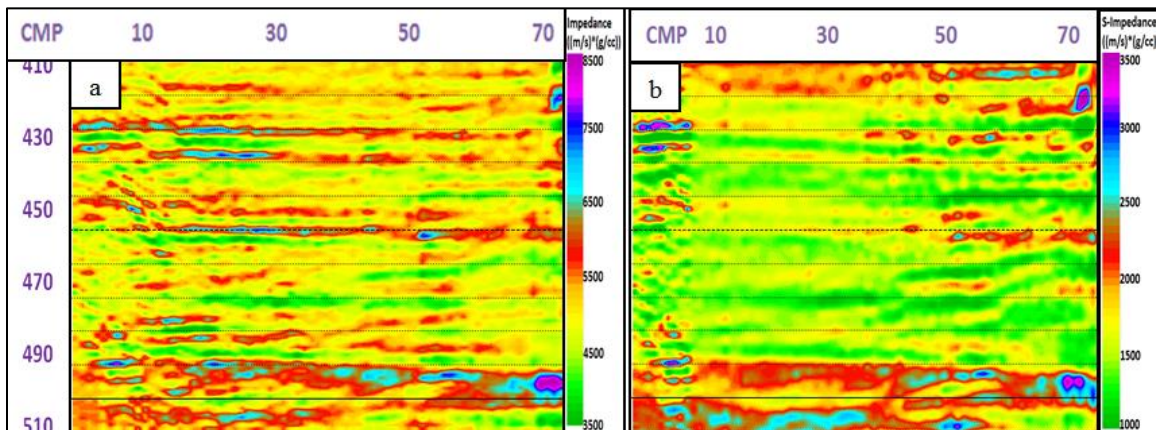


FIG. 18. Inverted Z_p and Z_s from R_p and R_s .

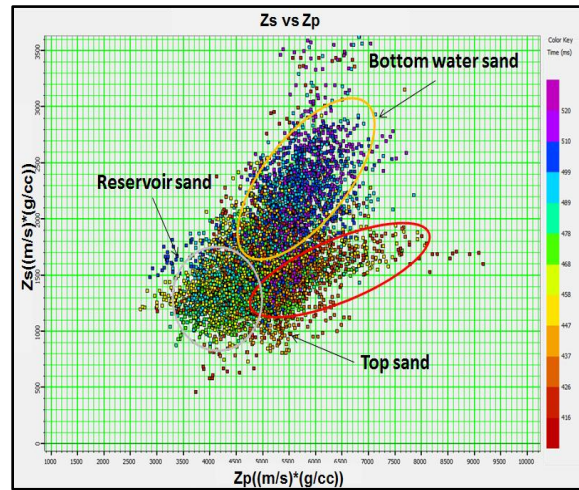


FIG. 19. Zs vs Zp crossplot.

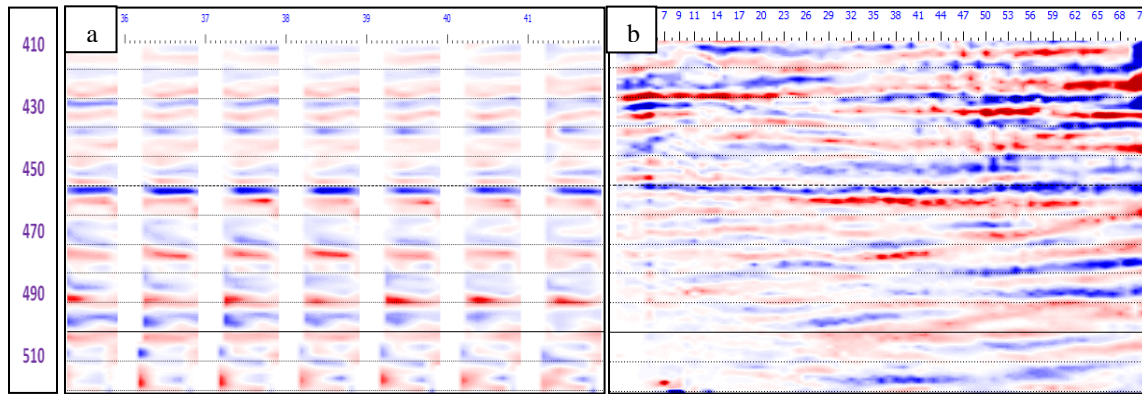


FIG. 20. (a) Angle gather and (b) fluid factor ($V_p/V_s=2.0$) inverted from two-term Fatti equation.

AVO LMR analysis:

From inverting the R_p and R_s , we can obtain Lambda-Rho (LR) and Mu-Rho (MR) which are shown in Figure 21. If there is gas effect, we would expect to see a significant decrease in LR volume and slight increase in MR volume.

A $\lambda\rho$ vs $\mu\rho$ crossplot (Figure 22) may minimize the effects of density and help to interpret the λ and μ attributes: the λ term (incompressibility) is sensitive to pore fluid therefore is an indicator of water vs gas saturation; whereas the μ term (rigidity) is sensitive to rock matrix and is used to help pure rock fabric or lithology (Satinder, et al., 2003). The samples highlighted by yellow rectangle have negative $\lambda\rho$ value which caused by noise. The red rectangle zone should be potential gas zone with low λ but high μ . Since there are only few samples in this area, it evidenced that no gas effects in the study reservoir. However, convincing cluster patterns can be seen in this crossplot. For example, the samples from the overlying shale are highlighted by the grey circle with low compressibility and low rigidity; samples from the reservoir top(sand) are highlighted by red ellipse with slightly higher incompressibility and rigidity; samples from the reservoir sand are highlighted by blue ellipse which show very low incompressibility and rigidity; samples from the bottom water sand are highlighted by yellow circle which show similar

incompressibility as the top reservoir sand but slightly higher rigidity. LMR is an effective tool to predict lithology and fluid in the study reservoir.

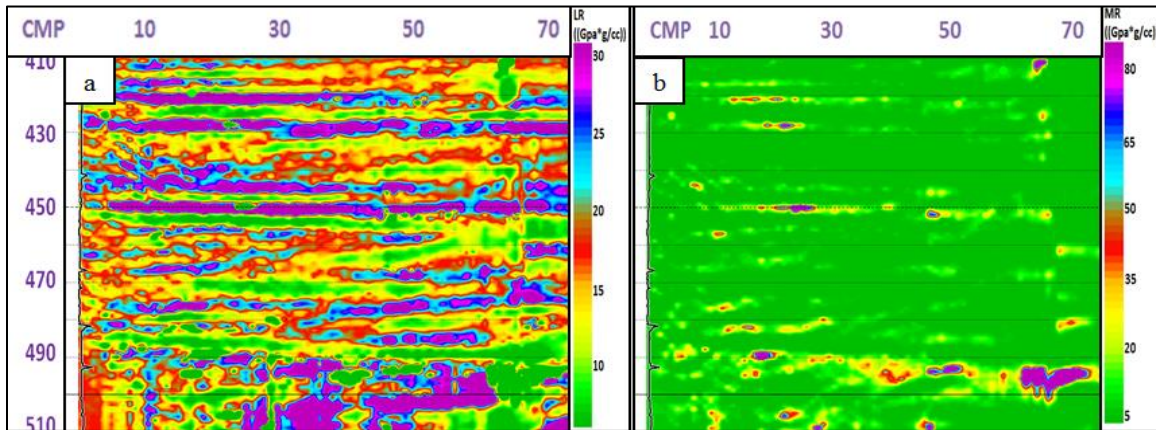


FIG. 21. Inverted Lambda Rho and Mu Rho.

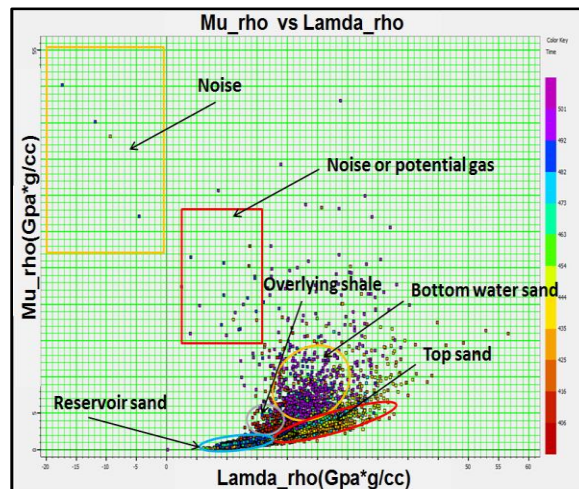


FIG. 22. Mu-rho vs Lambda_rho crossplot.

AVO modeling

As we discussed before, the V_p/V_s values were used from an adjacent well which is approximately 500m away from the VSP well. Then shear wave velocities and Poisson's ratio were calculated based on the V_p/V_s ratio. Also, the shear wave velocity and Poisson's ratio were estimated by AVO modeling and compared to calculated values. Two methods gave consistent results.

We modeled different fluid combinations based on the Biot-Gassmann's equation. Figure 23 shows the AVO modeling result. Figure 23a shows modeled logs. Logs in different colours were estimated from different scenarios. Blue curves represent pure brine, pink curves represent pure oil scenario and yellow curves are represent pure gas scenario. Black curves are from 80% brine and 20% oil scenario which is very close to pure brine and original logs. With pure gas (yellow curves), P wave, density and Poisson's ratio all show huge deviation from original logs.

In addition, we also modeled mixed gas saturation scenario which is shown by dotted dark green line. We saw dramatically decrease of P wave velocity and big change of Poisson's ratio even if we only saturated the reservoir with 5% gas. The modeling verified that there isn't gas effect in the study reservoir.

The observation was also validated by the synthetic gathers which is shown on Figure 23b. Gathers from pure gas and 5% gas scenario show strong amplitudes and they are increasing with offset. Gather from 80% of brine and 20% of oil scenario shows most close signatures with the VSP gather. Therefore, a good estimation from seismic is, the studied reservoir contains around 20% oil with 80% water, without gas effects.

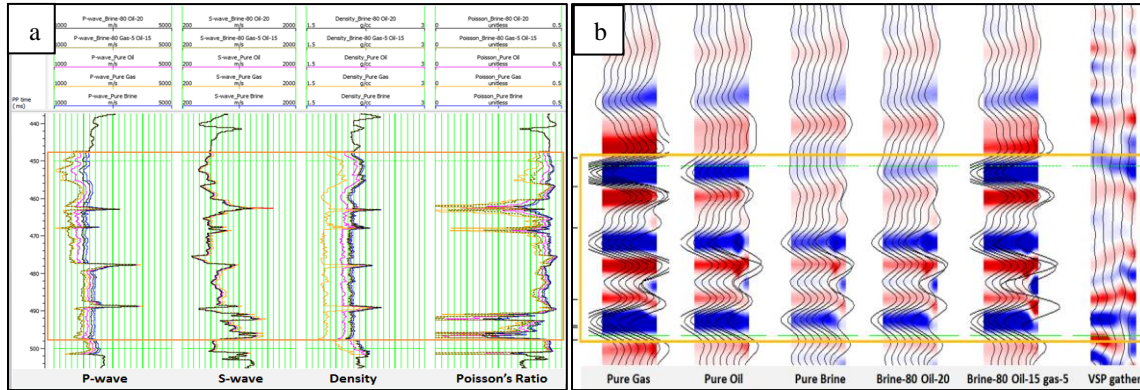


FIG. 23. AVO modeling result. (a) Estimated logs and (b) comparison of synthetics created in different scenarios and the VSP gather. The reservoir zones are highlighted by yellow rectangle. In (a), from left to right are P wave, shear wave, density and Poisson's ratio logs. In (b) from left to right are: synthetic from pure gas, pure oil, pure brine, 80% brine and 20% oil, 80% brine with 15% oil and 5% gas, field VSP gather.

Estimation from AVO modeling is compared to the production data which is listed Table 4. From the table, we can see that from 1984 to 1985, the total production of gas is $8 \text{ c}^3\text{m}^3$ and it is only about 0.05% of total production. The produced water is about 93%. From AVO modeling, we estimated the reservoir contains approximately 80% water, 20% oil, 0% gas. Since the well applied in the interpretation was logged in 1981 which is before the steam injection and production, the oil content may be overestimated and water may be underestimated. The study well was injected with steam of 13994 m^3 from 1984/02 to 1985/12. The error of estimated fluid may also occur from cooling down of injected steam, which may become water. In addition to that, the oil volume may shrink when the dissolved gas comes out. Considering all the aspects cause errors, our estimations of fluids from the VSP in the study reservoir are acceptable.

Table 4. Production of Well A, Clear-water formation

	Gas (c^3m^3)	Oil(m^3)	Water (m^3)	Gas%	Oil%	Water%
F12 Mo Prod	0	434	7443	0%	5.5%	94.5%
L12 Mo Prod	8	641	7267	0.1%	8.1%	91.8%
Cumulative Prod	8	1075	14710	0.05%	6.81%	93.14%

PP-PS joint inversion:

Joint PP-PS inversion can provide additional value and reduce risk or uncertainty in fluid/lithology discrimination and reservoir characterization. Figure 24 shows PP-PS registration. Reservoir zone is highlighted by a yellow rectangle. From the PS image, we can see that the low fold of far offset makes PS image less reliable in that zone. Figure 25 shows PP-PS joint inversion results. In general, the joint inversion results show lower resolution compared with P-wave inversion. It was caused by lower resolution of the PS image. The low resolution also degraded reliability of joint inversion results. Compared impedance from joint inversion to previous inversion results, they all show similar characteristics. All the P-impedance sections show lower P-impedance value inside the reservoir while the S-impedance doesn't change. It indicates that the shear wave velocities have little or no changes when the reservoir saturated with fluid. It also implies that the reservoir has no gas effects. Stable density and decreasing Vp/Vs values validated the interpretations.

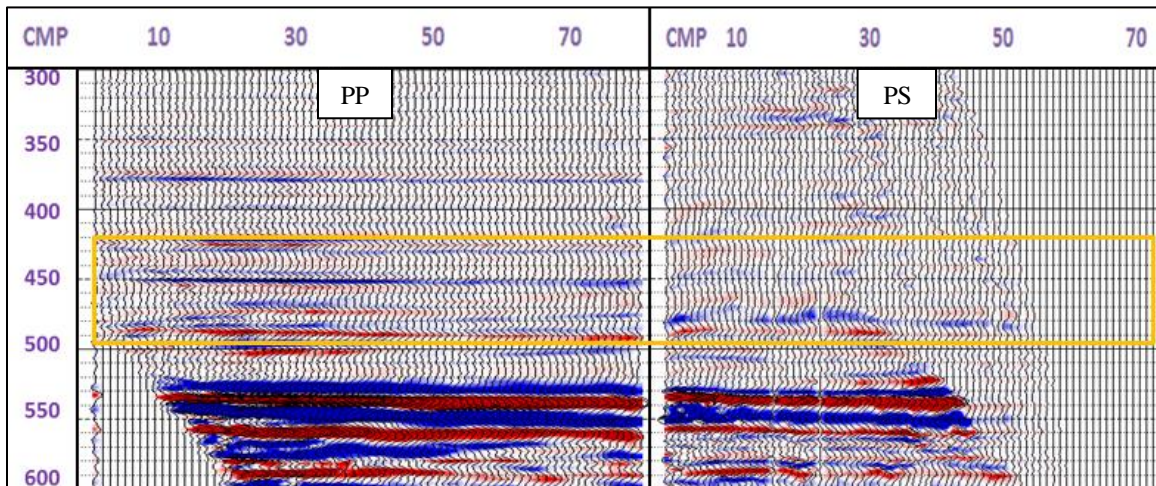


FIG. 24. Registration of PP and PS data. Reservoir zone is highlighted by a yellow rectangle.

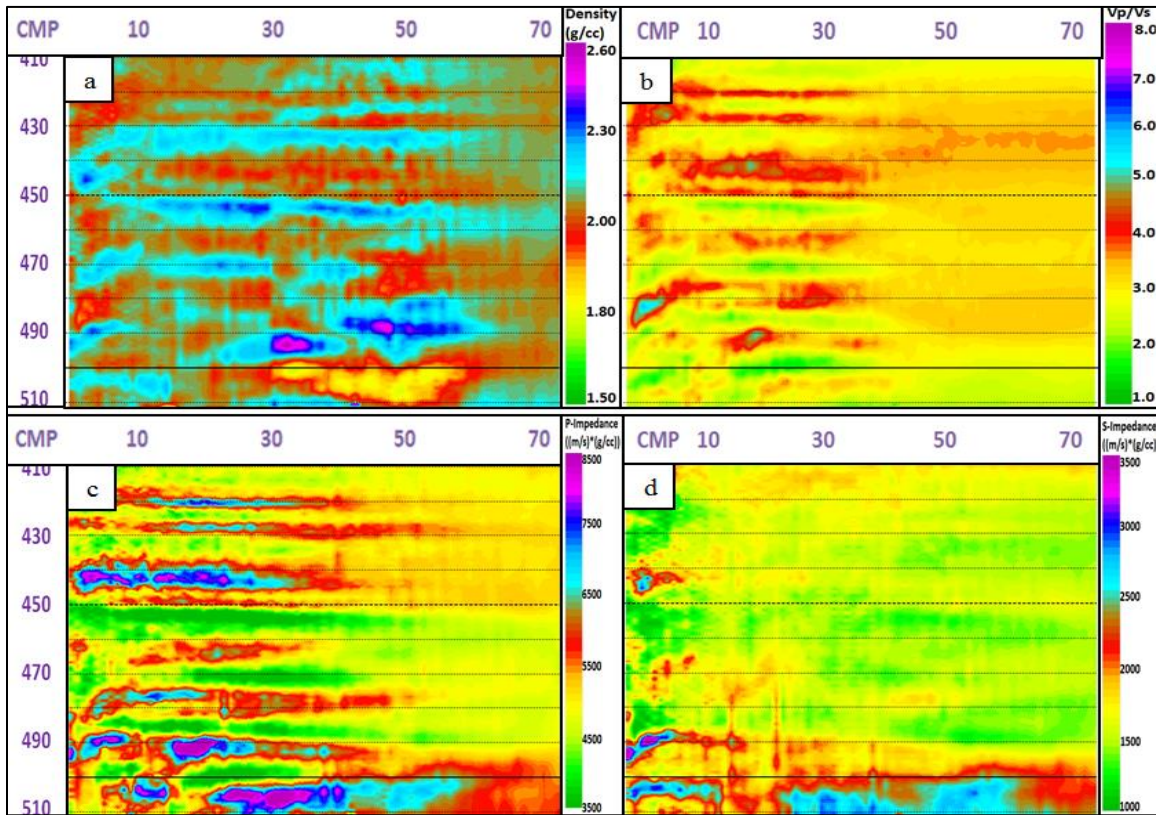


FIG. 25. Inverted (a) density, (b) V_p/V_s , (c) Z_p , (d) Z_s from PP-PS joint inversion.

Figure 26 is crossplot of S-impedance vs P-impedance inverted from PP-PS joint inversion. Compared with the P-wave only inversion result (Figure 19), this crossplot shows that the samples from overlying shale, top sand, reservoir sand and bottom water sand are in different locations. This distribution may be another indicator of lithologies and hydrocarbons. Overlying shale shows high Z_s/Z_p while top sand shows low Z_s/Z_p . Compared to the top sand, the bottom reservoir sand shows increasing Z_s/Z_p which may be caused by oil and water.

Figure 27 shows crossplots of V_p/V_s vs P-impedance and S-impedance inverted from PP-PS joint version. Again, the samples from the entire reservoir locate in four major zones while this distribution doesn't show on P-wave inversion crossplot (Figure 9). We can easily identify overlying shale, reservoir top sand, reservoir sand and bottom water sand on those crossplots. The information from S-wave data improved accuracy of prediction of lithology and fluid in the study reservoir.

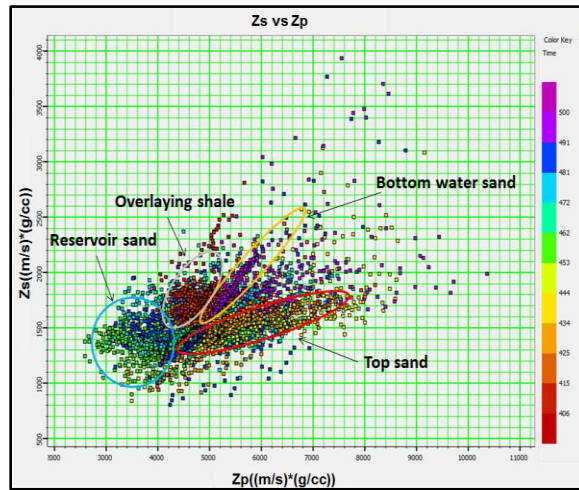


FIG. 26. Crossplot of S-impedance vs P-impedance inverted from PP-PS joint inversion.

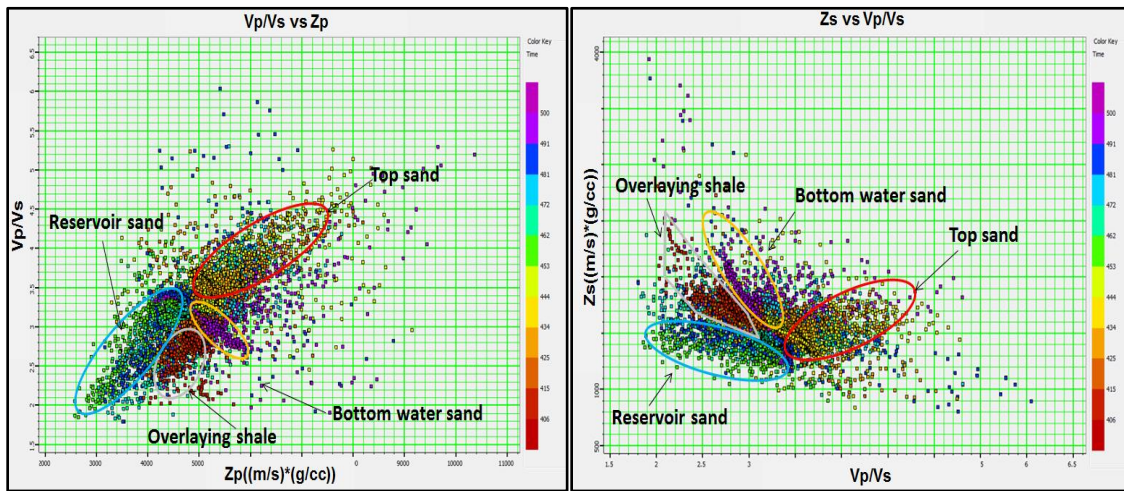


FIG. 27. (a) Crossplot of Vp/Vs vs P-impedance inverted from PP-PS joint inversion. (b) Crossplot of S-impedance vs Vp/Vs inverted from PP-PS joint inversion.

SUMMARY

Due to the advantage of VSP geometry, the hydrocarbon effects may be more visible on VSP data than surface seismic sections. In this work, we successfully applied VSP data analysis to predict rock properties and monitor production. P and shear wave impedance, reflectivity, Vp/Vs ratio and density were inverted from post stack and pre-stack inversion. Those properties are related to changes in the sedimentary environment and constrain the AVO responses. AVO analysis and modeling showed no obvious gas effects in the study interval which was validated by production data. PP-PS joint inversion added value to P-wave only interpretation. Inverted rock properties and their crossplots, AVO Lambda-mu-rho analysis are effective tools to predict lithologies and hydrocarbon in the study reservoir. However, the lower resolution of shear wave image and the distance of study well and VSP borehole as well as absence of shear wave log may degrade the reliability of the detailed interpretation.

ACKNOWLEDGEMENTS

We thank an anonymous company for providing the VSP data for this research and for permission to publish the results. We thank GEDCO/Schlumberger for providing the VISTA software and technical support during the data processing. We also thank CGG/Hampson-Russell for their inversion and AVO software. Finally, we give thanks to all of the CREWES sponsors for support of this research. We also gratefully acknowledge support from NSERC (Natural Science and Engineering Research Council of Canada) through the grant CRDPJ 379744-08.

REFERENCES

- Bubshait, S., 2010, VSP processing for coal reflections: M.Sc. Thesis, University of Calgary.
- Carcione, J. M. and Cavallini, F., 2002, Poisson's ratio at high pore pressure: *Geophysical Prospecting*, **50**, 97-106.
- Castagna, J. P. and Backus, M. M., Eds., 1993, Offset-dependent reflectivity—Theory and practice of AVO analysis: Soc. Expl. Geophysics.
- Castagna, J. P., Batzle, M. L., and Eastwood, R. L., 1985, Relationships between compressional-wave and shear-wave velocities in clastic silicate rocks: *Geophysics* **50**, 571–581.
- Castagna, J. P., Swan, H. W., and Foster, D. J., 1998, Framework for AVO gradient and intercept interpretation: *Geophysics*, **63**, 948–956.
- Chopra, S., Alexeev, V., Xu, Y., 2003, Successful AVO and Cross-plotting: Canada CSEG recorder, **28** No. 09.
- Coulombe, C.A., Stewart, R.R., and Jones, M.J., 1996, AVO processing and interpretation of VSP data: *Canadian Journal of Exploration Geophysics*, **32**, 41-62.
- Fatti, J.L., Smith, G.C., Vail, P.J., Strauss, P.J., Levitt, P.R., 1994, Detection of gas in sandstone reservoirs using AVO analysis: *Geophysics*, **59**, 1362-1376.
- Gassmann, F., 1951, Uber die Elastizitat poroser Medien: *Vierteljahrsschrift der Naturforschenden Gesellschaft in Zurich*, **96**, 1-23.
- Greenberg, M. L. and Castagna, J. P., 1992, Shear-wave velocity estimation in porous rocks: theoretical formulation, preliminary verification and applications: *Geophysical Prospecting*, **40**, 195-209
- Goodway, B., Chen, T. and Downton, J., 1997, Improved AVO fluid detection and lithology discrimination using Lamé petrophysical parameters; $\lambda\rho$, $\mu\rho$ and λ/μ fluid stack from P and S inversions: CSEG National Convention Expanded Abstracts, 148-151.
- Goodway, B., 2001, AVO and Lamé constants for rock parameterization and fluid detection: CSEG Recorder, 26, no. 6, 39-60.
- Hall, K. W., Lawton, D. C., Holloway, D., and Gallant, E.V., 2012, Walkaway 3C-VSP, CREWES Research Report, Volume 24.
- Hardage, B. A., 1983, Vertical seismic profiling-principles (1st ed.): Amsterdam, Geophysical Press Inc.
- Hein, F., Weiss, J., and Berhane, H., 2007, Cold Lake Oil Sands Area: Formation Picks and Correlation of Associated Stratigraphy: The Alberta Energy and Utilities Board/ Alberta Geological Survey (EUB/AGS) Geo-Note, 2006-03.

- Hinds, R.C., Kuzmiski, R.D., Botha, W.J., and Anderson, N.L., 1989, Vertical and lateral seismic profile, in Anderson N.L., Hills, L.V. and Cederwall, D.A., Eds., *Geophysical Atlas of Western Canadian Hydrocarbon Pools*, CSEG/CSPG, 319-344.
- Hinds, R.C., Anderson, N.L., and Kuzmiski, R.D., 2007, *VSP interpretative processing: Theory and practice*, SEG Continuing Education Course Notes.
- Hinds, R.C., and Kuzmiski, R.D., 2001, *VSP for the interpreter/processor for 2001 and beyond: part1*, CSEG Recorder, **26**, No.9, 84-95.
- Lawton, D.C, Gary, M. F., and Stewart, R. R., 2012, *Reflections on PS: An interactive discussion of problems and promise in converted-wave exploration: CREWES Research Report*, 24, 58.
- Lines, L.R., and Newrick, R.T., 2004, *Fundamentals of geophysical interpretation*, Geophysical Monograph Series: Society of Exploration Geophysicists.
- Margrave, G.F., 2008, *Methods of seismic data processing: Geophysics 557 Course Lecture Notes*, Department of Geology and Geophysics, University of Calgary.
- Ross, C.P., AND Kinman, D., L., 1995, *Nonbright spot AVO: Two Examples: Geophysics*, **60/5**, 1398-1408.
- Rutherford, S. R. and R. H. Williams, 1989, *Amplitude-versus-offset variations in gas sands: Geophysics*, **54**, 680–688.
- Simm, R., and Bacon, M., 2014, *Seismic Amplitude- an Interpreters Handbook*: Cambridge University Press.
- Smith, G. C., and Gidlow, P. M., 1987, *Weighted stacking for rock property estimation and detection of gas: Geophysics Prospecting*, **35**, 993-1014.
- Shuey, R. T., 1985, *A simplification of the Zoeppritz equations: Geophysics* **50**, 609–614.
- Wiggins, J.W., Ng, P., and Mazur, A., 1986, *The relation between the VSP-CDP transformation and VSP migration: 55th Ann. Internat. Mtg., SEG Expanded Abstract*.
- Wu, B., Lawton, D.C, and Hall, K., 2014, *Analysis of multicomponent walkaway vertical seismic profile data: CREWES Research Report*, 26, 79.
- Xu, C., and Stewart, R. R., 2003, *Ross Lake 3C-3D seismic survey and VSP, Saskatchewan: A preliminary interpretation: CREWES Research Report*, 15, 58.
- Zhang, John J. and Bentley, Laurence R., 2005, *Factors determining Poisson's ratio, CREWES Research Report*, 17, 62.